Molecular Mechanisms Underlying Medium-Chain Length Free Fatty Acid-regulated Activity of the Phospholipase PlaF from *P. aeruginosa*

Rocco Gentile[1], Matea Modric[2], Björn Thiele[3], Karl-Erich Jaeger[2,4], Filip Kovacic[2], Holger Gohlke[1,5]

1. Institute for Pharmaceutical and Medicinal Chemistry, Heinrich Heine University Düsseldorf, 40225 Düsseldorf, Germany
2. Institute of Molecular Enzyme Technology, Heinrich Heine University Düsseldorf, Forschungzentrum Jülich GmbH, 52425 Jülich, Germany
3. Institute of Bio- and Geosciences (IBG-2: Plant Sciences and IBG-3: Agrosphere), Forschungzentrum Jülich GmbH, 52425 Jülich, Germany
4. Institute of Bio- and Geosciences (IBG-1: Biotechnology), Forschungzentrum Jülich GmbH, 52425 Jülich, Germany
5. Institute of Bio- and Geosciences (IBG-4: Bioinformatics), Forschungzentrum Jülich GmbH, 52425 Jülich, Germany

Running title: Product feedback regulation of Phospholipase A PlaF

Keywords: molecular dynamics simulations, membrane, dimerization, tilting, potential of mean force

*Corresponding author:
Prof. Dr. Holger Gohlke
Institute for Pharmaceutical and Medicinal Chemistry
Heinrich Heine University Düsseldorf,
Universitätstr. 1
40225 Düsseldorf, Germany
and
Institute of Bio- and Geosciences (IBG-4: Bioinformatics)
Forschungzentrum Jülich GmbH,
Wilhelm-Johnen-Str.
52425 Jülich, Germany
Email: gohlke@uni-duesseldorf.de or h.gohlke@fz-juelich.de

ABSTRACT

PlaF is a membrane-bound phospholipase A1 from *Pseudomonas aeruginosa* that is involved in the remodeling of the membrane phospholipid composition. It modulates virulence-associated signaling and metabolic networks, although it remains unclear whether *P. aeruginosa*'s physiological changes are elicited by altered phospholipid composition or by free fatty acids (FFAs) released from phospholipids. Previously, we identified that undecanoic acid bound to the active site of PlaF in the crystal structure inhibits PlaF activity and triggers the formation of PlaF dimers. However, the detailed molecular mechanism governing the inhibition and dimerization of PlaF by medium-chain length FFAs has remained elusive. In this study, we used unbiased and biased molecular dynamics simulations and free energy computations to assess how FFAs localized in different cell compartments can interact with active and inactive configurations of PlaF and how this may regulate *PlaF* activity. Our results suggest that medium-chain length FFAs can inhibit PlaF both competitively and non-competetively, in line with previous experiments. They stabilize inactive dimeric PlaF when localized in the upper membrane leaflet and enter a tunnel connected to the catalytic triad when localized in the periplasmic space. We predict mutations for either case to probe these effects experimentally. Our findings support the suggestion from *in vivo* results shown here and *in vitro* results presented previously that PlaF activity may be regulated through a product-feedback mechanism. They also open up new perspectives on how to inhibit PlaF, which has been suggested as a promising target for developing new antibiotics against *P. aeruginosa*.

1. INTRODUCTION

The Gram-negative bacterium *Pseudomonas aeruginosa* is an opportunistic pathogen and a frequent cause of nosocomial infections, affecting primarily immune-compromised patients (1, 2). The pathogenicity of *P. aeruginosa* relies on the production of a large spectrum of virulence factors (3). Among these, type A phospholipases (PLA_1) are bacterial proteins that can contribute to host membrane damage and trigger the deregulation of various signaling networks in infected cells (4). PLA_1 hydrolyzes membrane glycerophospholipids (GPLs) at the *sn*-1 position into lysoglycerophospholipids (LGPLs) and free fatty acids (FFAs) (5, 6). GPLs are membrane components involved in cellular integrity and membrane protein stability (7). The alteration of the membrane GPL composition has been linked to the biofilm formation and growth phase transitions in *P. aeruginosa* (1, 2, 8).

PlaF is a newly discovered transmembrane phospholipase A1 (PLA1) of *P. aeruginosa* that contributes to the virulence of this bacterium and is involved in the modulation of the pathogen membrane composition (3, 4). A crystal structure of PlaF, combined with homodimerization studies by crosslinking, micro-scale thermophoresis experiments, and molecular simulations has revealed that PlaF can adopt both monomeric and dimeric configurations **(Figure 1)** (5)**.** However, only the monomeric state of the protein was found to be catalytically active. The crystal structure revealed a homodimer characterized by interactions between the transmembrane (TM) and juxtamembrane (JM) regions between the single monomers. The crystal structure contains the co-crystallized endogenous ligands myristic acid (MYR) and undecanoic acid (11A) in the catalytic site of each monomer (5).

Free energy computations (9) and experiments indicated that, at physiological protein concentrations, the equilibrium between the PlaF dimer and the monomers is shifted to the latter side (5). Unbiased molecular dynamics simulations (10) showed that the PlaF monomer undergoes a tilting motion in the membrane, bringing the opening of the catalytic tunnel in close vicinity to the membrane (5). In the dimeric form, the tunnel entrance resides more than 5 Å above the membrane's upper leaflet, thus hampering phospholipid substrate access from the membrane (5). Moreover, free energy computations revealed that the tilted state (t-PlaF) of the monomeric PlaF is energetically more favorable than the non-tilted one. As a result, it has been suggested that this tilting motion underlies the activation of the monomeric PlaF by facilitating substrate access to the active site tunnel (5).

In addition to the previously mentioned tunnel (T1), two other tunnels (T2 and T3) were identified, connecting the active site to the surface of PlaF (11). Unbiased MD simulations showed that myristic acid (MYR), the hydrolysis product of 1-myristoyl-2-hydroxy-*sn*-glycerol-3-phosphoglycerol (2LMG), a lysophospholipid, relocates from T3 and reaches the entrance of T1. Interestingly, MYR is also found in T1 in the crystal structure of PlaF (5, 11). Accordingly, the fatty acid can reach the membrane, where it might modify its composition and properties. Furthermore, the FFA might carry out its role as a signal molecule of the diffusible signal factor (DSF) or oxylipin autoinducer (12) families, important for bacterial virulence in the pathogen (13).

A recent study showed that medium-sized FFAs (10-14 carbon atoms) inhibit PlaF activity according to a mixed inhibition mode and that they lead to an increase in the PlaF dimer concentration (5). Experiments also revealed that FFAs with 10-14 carbon atoms can inhibit PlaF in competitive inhibition assays (5). We hypothesize that the FFAs inhibit PlaF activity in two ways: I) when located in the membrane, they impact the dimer-monomer equilibrium and/or the tilting transition, that way acting as an allosteric inhibitor; II) when located in the periplasmic space, they enter T3 and reach the active site, that way acting as a competitive inhibitor **(Figure 1).** However, the detailed molecular mechanisms that govern the PlaF inhibition by FFAs have remained elusive.

To investigate such mechanisms, we combine unbiased and biased all-atom molecular dynamics (MD) simulations (14) and configurational free energy computations (9) to evaluate the effect of FFAs on the structural dynamics and energetics of the PlaF dimer-monomer transition and the monomer tilting. To

reveal hot spot residues potentially involved in the interaction of FFAs with PlaF, we used MM-PBSA endpoint free energy calculations (15). Additionally, we pursue free ligand diffusion MD simulations (16) and binding free energy computations (9) of FFAs located in the water phase near the catalytic domain of PlaF. The identification of FFA binding site(s) involved in PlaF inhibition might help to design novel drugs against *P. aeruginosa*.

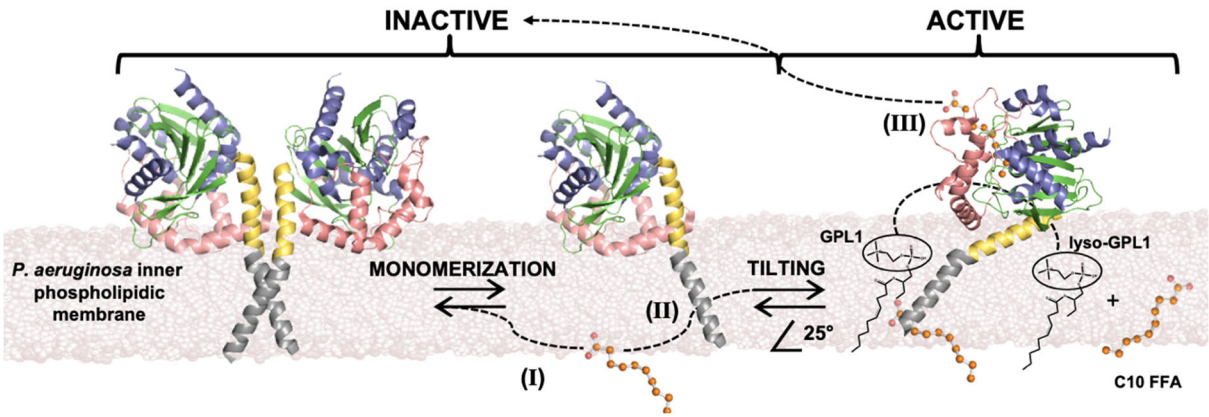

Figure 1. Dimer-monomer equilibrium of PlaF, monomer tilting, and putative influence by FFA. PlaF is anchored to the inner membrane through a transmembrane (TM) region (grey) containing lipophilic residues and a juxtamembrane (JM) region (yellow) that is in close contact with the polar heads of the phospholipid membrane when PlaF is tilted. This region is rich in polar and charged residues. The C-terminal region (green, violet, pink) points towards the periplasm. It is characterized by an α/β hydrolase fold and contains the catalytic triad (Ser, Asp, His) that catalyzes the GPL hydrolysis. PlaF can adopt a dimeric or monomeric configuration (left), and the monomer can tilt (right). The tilted monomer is considered the active form (5). FFA may influence the dimer-monomer equilibrium (I) and/or the tilting transition (II) and/or enter PlaF from the periplasm (III). GPL1, glycerophospholipid; lyso-GPL1, lysoglycerophospholipid; C10 FFA, decanoic acid.

2. RESULTS

2.1 Medium-chain Fatty Acids are Detected in *P. aeruginosa* in Free Form and Likely Originate from Phospholipid Hydrolysis

Our previous lipidomics analysis by Q-TOF MS/MS revealed that the alteration of the membrane phospholipid composition in *P. aeruginosa* is linked to PlaF-mediated degradation of several phospholipids (PLs), including three PLs containing medium-chain FAs: phosphatidylglycerol (PG) 24:3, phosphatidylethanolamine (PE) 22:1, and phosphatidylinositol (PI) 26:0 (5). In this study, we analyzed if medium-chain FFAs can be identified in *P. aeruginosa* wild-type (WT) and an isogenic *plaF* mutant (Δ*plaF*) with reduced PL degradation. To achieve this, we extracted FFAs from cells and supernatant of both strains using organic solvent and quantified the saturated FFAs with acyl chains of six to 16 carbon atoms by GC-MS. The results showed that both *P. aeruginosa* strains produced various intracellularly and extracellularly located saturated FFAs **(Figure 2)**. As anticipated, the long-chain FFAs were the most abundant, while medium-chain FFAs (C8, C9, C10, C12, and C14) accounted for roughly 10 to 15 % of the total FFA amount. No significant differences in the abundance of cell-associated FFAs between the WT and Δ*plaF* were observed, suggesting that FFAs released by PlaF are either metabolized or secreted into the supernatant. We identified that medium-chain FFAs, namely octanoic (C8), decanoic (C10), dodecanoic (C12), and myristic (C14) acids, were significantly less abundant ($p < 0.05$) in the supernatant of Δ*plaF* than the WT.

To further explore the possibility that PlaF releases the identified medium-chain FAs from PLs, we conducted a re-analysis of our published lipidomics results obtained with the Δ*plaF* mutant (5). Our previous analysis had assessed PLs at the species level, meaning that only information about the total number of carbon atoms in the acyl chains but not their specific identities were obtained. Thus, we focused on PL species with up to 24 carbon atoms in their acyl chains, as they likely contain at least one medium-length acyl chain (**Table S1**). Our results showed that the *P. aeruginosa* membrane contains 56 different medium-chain length PLs out of a total of 324 identified PL species (**Table S1**). A comparison of the amount of medium-chain length PLs relative to the total PL amount in WT and Δ*plaF* revealed that more (20.8 %) medium-chain length PLs were identified in the Δ*plaF* mutant than the WT (12.6 %) (**Table S2**). These results suggest that medium-chain length PLs could potentially be the source of the suggested FFAs, generated by PlaF-catalyzed hydrolysis.

The GC-MS analysis revealed an interesting finding: the extracellular C8 FFA amount was nearly double ($p < 0.001$) that of the intracellular amount in both the WT and Δ*plaF* strains, suggesting that this FA is primarily secreted into the supernatant. In contrast, dodecanoic acid, the second FFA identified as a potential product of PlaF-catalyzed PL hydrolysis, was significantly ($p < 0.001$) more abundant in the cells of Δ*plaF* than the WT. These results reveal that the distribution of FFAs, whether they are intracellular or extracellular, is dependent on their chain length. This suggests that some FFAs may have a function as extracellularly secreted compounds, such as signaling messengers, while others may be primarily used intracellularly, such as for energy production.

To conclude, the quantification results of FFAs further strengthen the suggested *in vivo* function of PlaF in degrading PLs containing medium-length acyl chains. Previous *in vitro* results indicated that released FFAs may regulate PlaF activity through a product-feedback mechanism (5).

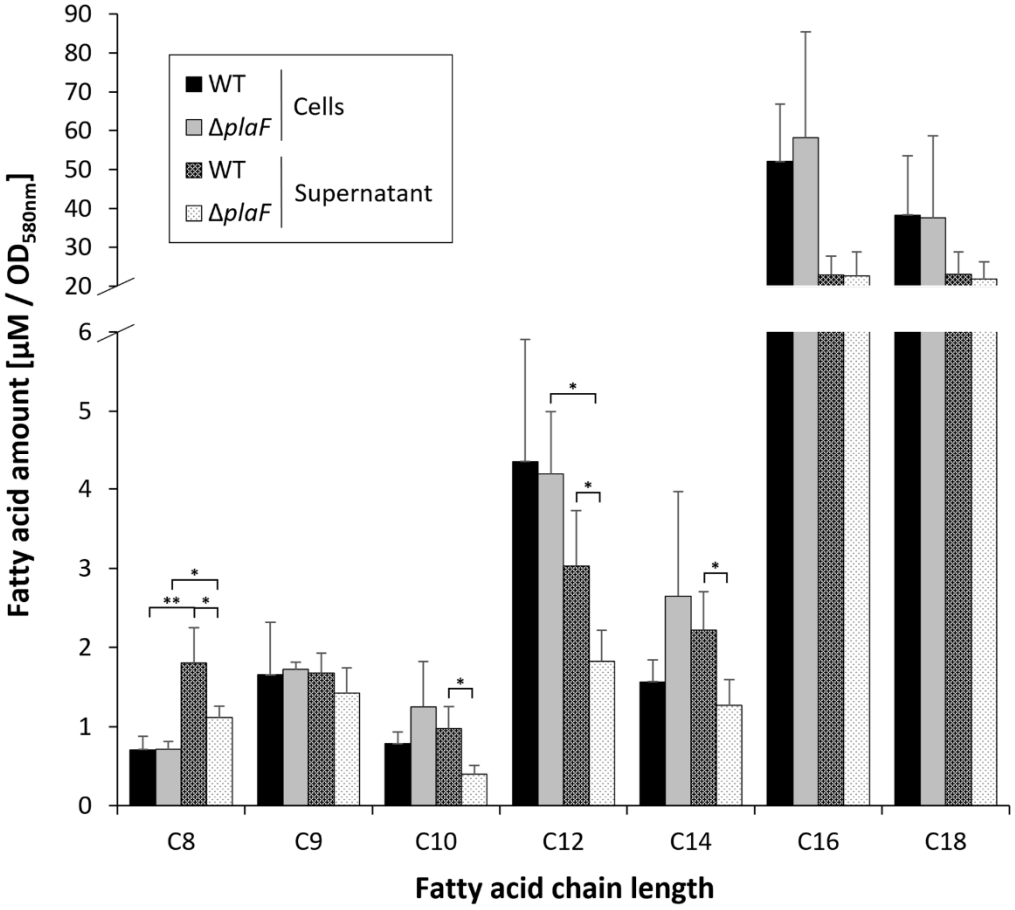

Figure 2: Free fatty acid profile of *P. aeruginosa* WT and Δ*plaF*. Strains were cultivated in LB medium under aeration until the stationary phase and FFAs were extracted with organic solvent from cells and supernatant. Quantification of FFAs was performed by GC-MS analysis. Means ± SDs are shown (n = 4 biological replicates). Statistical analysis was performed using the t-test, * $p < 0.05$, ** $p < 0.01$; remaining differences were not significant

2.2 Free Fatty Acids in the Membrane may Facilitate the Tilting of PlaF Monomers

We performed all-atom unbiased MD simulations (14) of monomeric PlaF with FFA molecules as membrane components, considering either the orientation of PlaF as obtained after splitting the membrane-embedded PlaF dimer (s-PlaF) or the tilted orientation obtained for the monomer with OPM (17, 18) (t-PlaF). For each PlaF configuration, two membrane systems were examined, in which decanoic acid (C10) or myristic acid (C14) was inserted in the upper leaflet of the inner phospholipidic membrane, resulting in a DOPE:DOPG:FFA composition of 3:1:1. This corresponds to the addition of 25 FFA molecules to either system and a 20 mol% FFA fraction in the upper leaflet. For each system, 12 replicas were simulated, each 1 µs in length. The results were compared with those obtained with a membrane composition without FFAs (DOPE:DOPG 3:1) (5).

When starting from the s-PlaF orientation, a comparable number of transitions to the t-PlaF orientation ("tilting") was observed for both systems containing FFAs (9/12 vs. 10/12) **(Figure 3)**, indicating that the latter orientation is preferred and the chain length has no influence on the tilting preference. The presence of FFAs may facilitate the tilting, however, as only 5/10 (8/10) transitions were observed after 1 (2) µs of simulation time for the system without FFAs (5). As before (5), when starting from the t-Plaf orientation, no transition to the s-PlaF orientation was observed **(Figure 3)**, supporting that the

former orientation is preferred. Extending the MD simulations to 2 μs does not lead to transitions in this case either **(Figure S1)**.

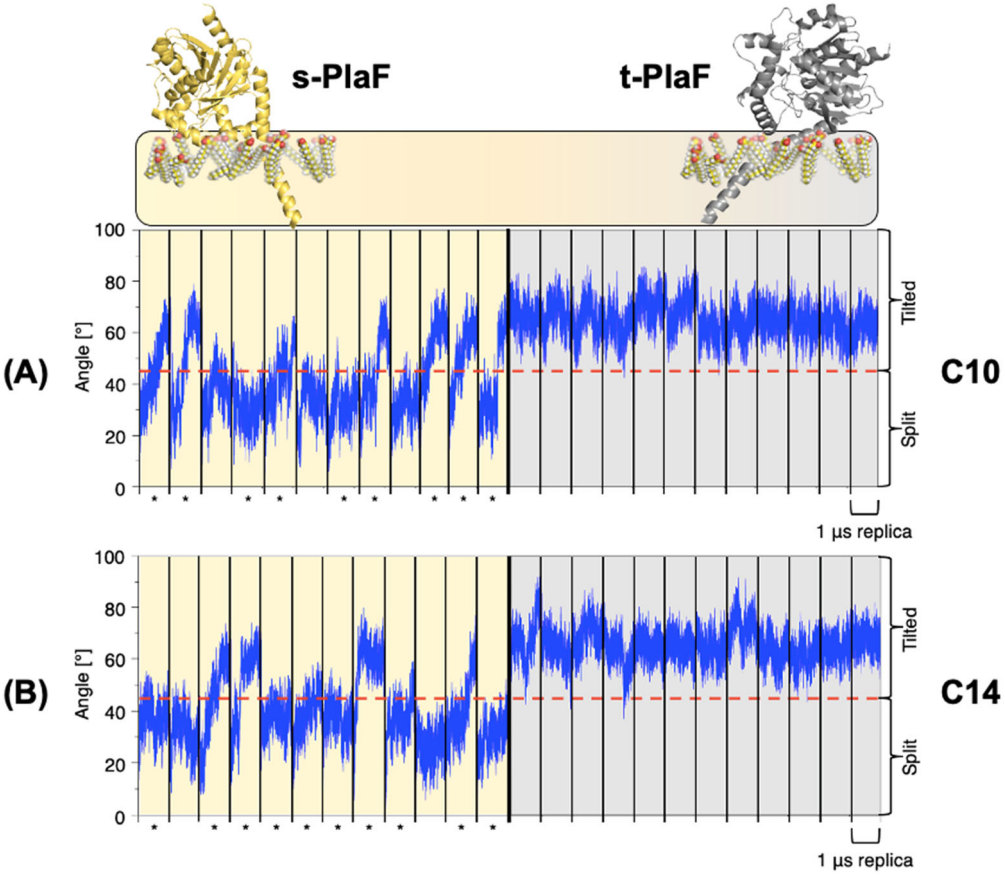

Figure 3. Unbiased MD simulations of monomeric PlaF in the presence of FFA in the upper leaflet (DOPE:DOPG:FFA of 3:1:1). (A) Left: Time course of the orientation of monomeric PlaF with respect to the membrane starting from the $PlaF_A$ configuration as observed in the structure (*s*-PlaF, see the top of the figure) in the presence of decanoic acid (C10). In 9 of 12 replicas, the monomer ends in a tilted configuration (marked with *). Right: When starting from t-PlaF (see the top of the figure), the structure remains tilted in all cases. As before (5), this shows a significant tendency of the monomer to tilt (McNemar's $\chi^2 = 6.125$, $p = 0.013$). The monomer orientation is quantified by the angle between the membrane normal and the vector between the COM of residues 21–25 and residues 35–38. **(B)** As in panel A, but now with myristic acid (C14). In 10 of 12 replicas, the monomer ends in a tilted configuration (marked with *), again showing a significant tendency of the monomer to tilt compared to when starting from the t-PlaF orientation (McNemar's $\chi^2 = 8.100$, $p = 0.004$).

2.3 Free Fatty Acids Favor Monomer Tilting but Disfavor Dimer Dissociation

To determine the effect of FFAs in the upper leaflet on the energetics of the PlaF dimer-to-monomer and s-PlaF-to-t-PlaF transitions, we performed umbrella sampling (US) simulations (19) to compute potentials of mean force (PMF) (20). As the chain length showed little influence on the tilting behavior in the unbiased MD simulations, we considered the membrane system with DOPE:DOPG:C10 for this purpose. The US simulations were performed as in ref. (5), starting from the monomer orientation as in the crystal structure (s-PlaF). The distance between the top of the JM domain (COM of residues 33-37) and the membrane center was used as a reaction coordinate to track the tilting transition. For the dimer-to-monomer transition, we started from the dimer configuration as found in the crystal structure and used the distance between the COM residues 25-38 of each chain as a reaction coordinate. For the tilting transition, 40 windows were sampled with 800 ns of sampling time each, of which the first 640 ns were discarded as equilibration. Likewise, for the dimer-to-monomer transition, 71 windows were sampled with 800 ns of sampling time each, of which the first 640 ns were discarded as equilibration. In both cases, the kernel densities showed a median overlap of 34.9 ± 1.4% and 32.2 ± 1.5% between contiguous

windows, respectively **(Figures S7 and S8)**, well suited for PMF calculations (21). The error was estimated by focusing on the last 160 ns of each window and calculating the standard error of the mean from free energy profiles determined independently every 20 ns.
The PMF of the titling transition is converged and precise **(Figure S7)**. In the presence of 20% C10 FFAs in the membrane, the tilted orientation is preferred over the split orientation **(Figure 4A)**, which is similar to results without FFA in the membrane (5). Unlike in the case without FFAs in the membrane (5), however, the tilted configuration reveals a more pronounced, ~4 kcal mol^{-1} more favorable basin. Additionally, another local minimum appeared where a barrier previously separated the split and tilted configurations in the system without FFA. These results are in accordance with the unbiased MD simulations, which indicated that the tilted configuration is preferred and that the transition to it is facilitated in the presence of FFAs.

The PMF for the dimer-to-monomer transition was computed considering two membrane compositions with 20 mol% and 30 mol% of FFA in the upper leaflet. The PMFs are converged and precise **(Figures S8 and S9)**. As in the case without FFA (5), dimeric PlaF is favored over the monomeric state in the presence of FFAs **(Figure 4B)**. However, the presence of FFA stabilizes the dimeric state in a concentration-dependent manner by ~10 and ~14 kcal mol^{-1} compared to no FFA.

To conclude, FFAs in the upper leaflet favor the tilting of the PlaF monomer and stabilize the PlaF dimer in a concentration-dependent manner **(Figure 4C)**.

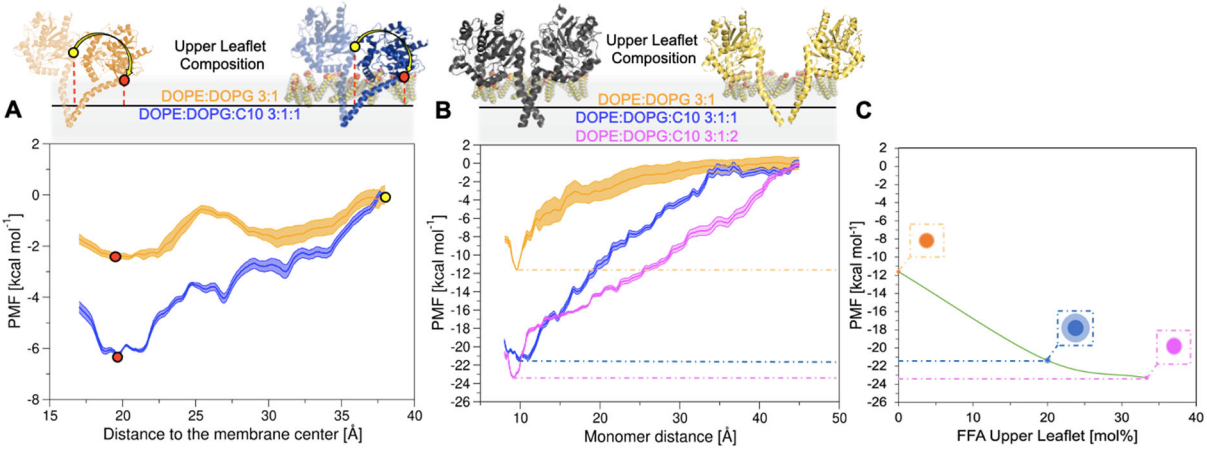

Figure 4. (A) Potential of mean force of monomer tilting. The distance between the COM of Cα atoms of residues 33–37 and the COM of the C18 of the oleic acid moieties of all lipids in the membrane was used as a reaction coordinate. Orange: PMF for the membrane composition in the upper leaflet of DOPE:DOPG 3:1 (values were taken from ref. (5)). Blue: PMF computed here for the membrane composition in the upper leaflet of DOPE:DOPG:C10 3:1:1. The shaded areas show the standard error of the mean (SEM). The yellow dot indicates the s-PlaF orientation, and the red dot the t-PlaF orientation. **(B) Potential of mean force of dimer separation.** The distance between the COM of C_α atoms of residues 25-38 of each chain was used as the reaction coordinate. Orange: PMF for the membrane composition in the upper leaflet of DOPE:DOPG 3:1 (values were taken from ref. (5)). Blue: PMF computed here for the membrane composition in the upper leaflet of DOPE:DOPG:C10 3:1:1. Magenta: PMF computed here for the membrane composition in the upper leaflet of DOPE:DOPG:C10 3:1:2. The shaded areas show the SEM. The black protein on the top show the PlaF dimer at ~9.9 Å, and the yellow ones show the completely dissociated PlaF at ~45 Å. **(C) PMF values at the respective global minima of panel B (see dashed lines there)** as a function of the C10 concentration in the upper leaflet. The shaded areas around each dot show the SEM at the corresponding minimum.

2.4 Estimating the ratio of monomeric and dimeric PlaF in the cell in the presence of free fatty acids

Following previous work by us (5, 22) and others (23), we computed from the PMFs of dimer-to-monomer and tilting transitions with an upper leaflet composition of DOPE:DOPG:C10 3:1:1

243 equilibrium constants (K_a = 1.68 x 10^{14} (eq. S1), K_x = 2.59 x 10^{12} (eq. S2), $K_{tilting}$ = 1.73 x 10^2 (eq. S5))
244 and free energies (ΔG = - 17.04 ± 0.22 (eq. S3), $\Delta G_{tilting}$ = - 3.04 ± 0.20 (eq. S6)), taking into account
245 that K_x and ΔG relate to a state of one PlaF dimer in a membrane of 1258 lipids, according to our
246 simulations setup. Experimentally, a concentration of one PlaF dimer per ~3786 lipids in *P. aeruginosa*
247 PlaF-overexpressing cells was determined (24). However, the concentration in *P. aeruginosa* WT is
248 likely 100- to 1000-fold lower. Under such physiological conditions and considering that the equilibria
249 for dimer-to-monomer transition and tilting are coupled, between 2.3 and 7.3% of the PlaF molecules
250 are predicted to be in a monomeric, tilted, catalytically active state in *P. aeruginosa* when 20 mol%
251 C10 FFAs are present in the upper leaflet. In the absence of FFAs, between 74% and 96% of the PlaF
252 molecules were predicted to be in a monomeric, tilted, catalytically active state in *P. aeruginosa* (5).

253 *Vice versa*, in the presence of FFA, 92.7 to 97.7% of PlaF are in the dimeric configuration, whereas this
254 are only 4 to 26% in the absence of FFA (5). The computed increase in the PlaF dimer concentration
255 agrees with previous global DMP-crosslinking experiments that showed an increased d-PlaF
256 concentration in C10-treated samples (5).

257 ### 2.5 Hot spots of d-PlaF – FFA Interactions in the Upper Leaflet

258 To characterize interactions between FFA in the upper leaflet (DOPE:DOPG:C10 3:1:1) and PlaF that
259 may favor dimer formation, we extracted snapshots from the trajectories of unbiased MD simulations
260 across 12 multiple replicas where FFA are located ≤ 6 Å away from the protein and that have an
261 RMSD < 1.5 Å to the previous pose (see Supplementary results). These poses were selected as stably
262 bound poses and clustered with respect to the minimum distance ε between the clusters used as the
263 cluster criterion. Starting from ε = 2.0 Å, we gradually increased ε in 0.5 Å intervals until the population
264 of the largest cluster remained unchanged (ε = 5.0 Å).
265 The five most populated clusters cover 80.5 ± 1.5% (mean ± SEM) of all snapshots with FFA close to
266 the protein and 65.8 ± 1.3% of all snapshots in a trajectory **(Figure 5A)**. Over these clusters, potential
267 interacting residues are identified based on a distance cutoff of ≤ 6.0 Å from the FFA clusters **(Figure**
268 **5B)**. These residues comprise more positively charged than negatively charged ones and are exclusively
269 located in the lid-like domain, where their sidechains can interact with the head groups of the FFA.
270 **(Figure 5B)**. These residues are suggested to be important for the stabilizing effect of FFA on the PlaF
271 dimer and shall be validated by mutagenesis and biochemical studies.

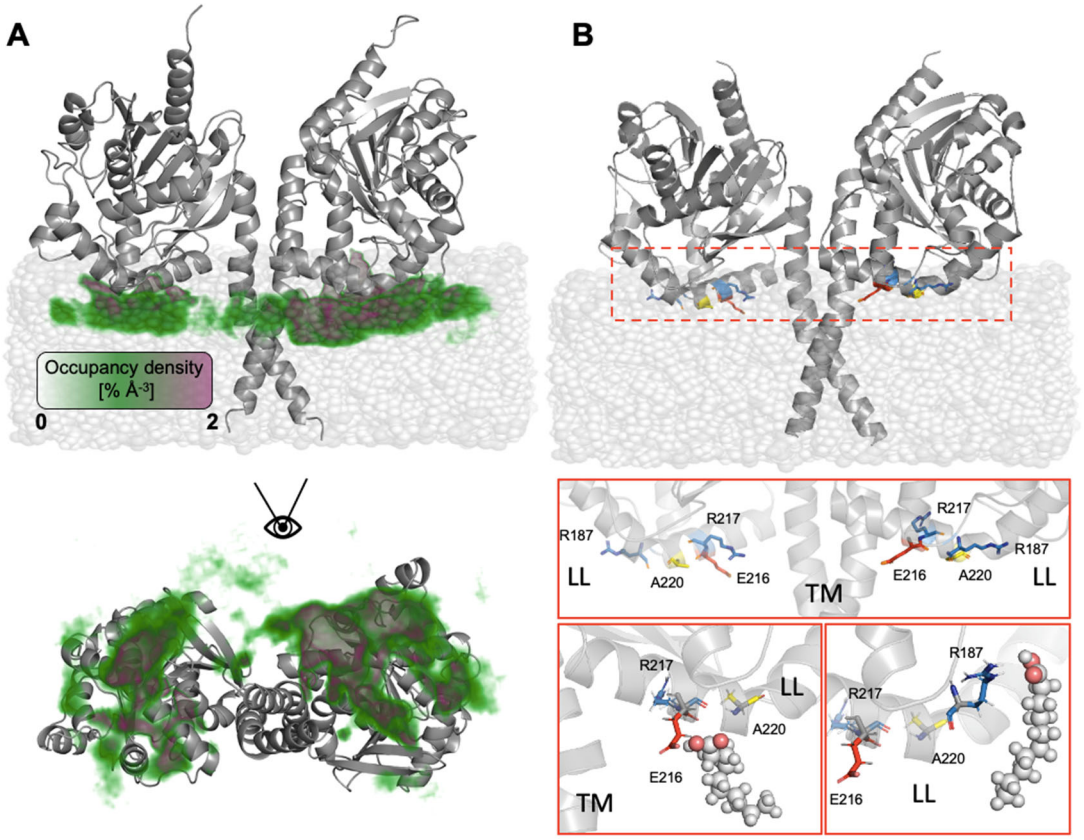

Figure 5. Hot spots of d-PlaF – FFA interactions when FFA are in the upper leaflet (DOPE:DOPG:C10 3:1:1). **(A) Average density map of all C10 molecules**. Top panel: Average density map of the entire C10 computed with CPPTRAJ (25); bottom panel: Average density map of the entire C10 molecules, shown from a 90° view. The fatty acids are close to both monomers in similar proportions. **(B) Hot spots of FFA binding to PlaF where C10 is ≤ 6 Å away from d-PlaF and has an RMSD < 1.5 with respect to the previous pose**. The negatively and positively charged hot spots are shown in red and blue sticks, respectively, while non-polar ones are reported in yellow sticks. The hot spots are localized on the lid-like (LL) domains of the two monomers and are suggested for mutagenesis studies. Of the lower panels, the top one is a blow-up of the interaction region marked as the dashed box. Below, two examples of FFA poses are reported. The left panel indicates the interaction of C10 with E216 and R217. The right panel indicates the interaction of C10 with R187. This is also an example of how interactions can involve a single fatty acid and multiple residues of PlaF. The fatty acid is reported as white spheres and residues as sticks.

2.6 Free Fatty Acids in the Periplasmic Space Interact with t-PlaF Primarily via Entering T3

Previous inhibition assays with FFA added to the soluble fraction in a 7.5 mM concentration revealed that the inhibition potency of FFAs on PlaF esterase activity increased with increasing FFA acyl chain length (in the range of 10-14 carbon atoms) (5). To understand how FFA in the water phase (mimicking the periplasmic space under physiological conditions) can influence PlaF activity, we investigated if such FFAs can bind to t-PlaF with all-atom MD simulations of free ligand diffusion (FLD) of 1 µs length (16). t-PlaF was embedded in a membrane with the composition DOPE:DOPG 3:1 mimicking the phospholipid composition of the *P. aeruginosa* inner membrane (5, 8). Furthermore, 10 molecules of FFA with chain lengths of 5 (valeric acid (VAC-C5)), 10 (capric acid (CAP-C10)), or 15 (pentadecanoic acid (PEN-C15)) carbon atoms were added in the water phase, resulting in concentrations of 30 mM in the solvation box each. A higher concentration than the experimentally used one was chosen to increase the probability of observing events of FFA binding to and dissociation from t-PlaF. As this concentration is above the CMC for each of the FFA (26), we monitored by visual inspection of the trajectories that no fatty acid aggregates formed.

For each of the three systems, 12 replicas were performed, and binding and unbinding events of the FFA were monitored **(Figure 6A)**. We identified an FFA as "bound" if it is within a distance < 15 Å from the T3 entrance (COM of residues K170, Q234, Y236) and has an RMSD < 1.5 Å to the previous pose (see Supplementary results) (11). Density maps of FFAs around t-PlaF show that FFAs tend to gather in T3, which connects the catalytic center to the periplasmic space **(Figure 6B)**. T3 has previously been suggested to play a role in relocating substrates within the catalytic center, which is necessary for the PLA1 activity of PlaF (11). Furthermore, it has been hypothesized that FFA may leave PlaF via T3 after lipid cleavage (11).

C5 molecules showed almost no binding into T3 (2.5 % binding events across all replicas). C5 inhibits PlaF to only 10.1 ± 2.3% (5). C10 and C15 showed a comparable number of binding events to T3 **(**26.7 and 27.5 %, respectively), **Figure 6A)**. Of these, ~80.0% access T3 in either case. In most instances, the FFA tail enters T3 first (**Figure 6C-D**), which is compatible with the mostly hydrophobic composition of T3 (11). In contrast to the similar binding behavior of C10 and C15 in FLD simulations, C10 inhibits PlaF activity more strongly (74.3 ± 3.3 %) than C15 (41.3 ± 2.2%) (5).

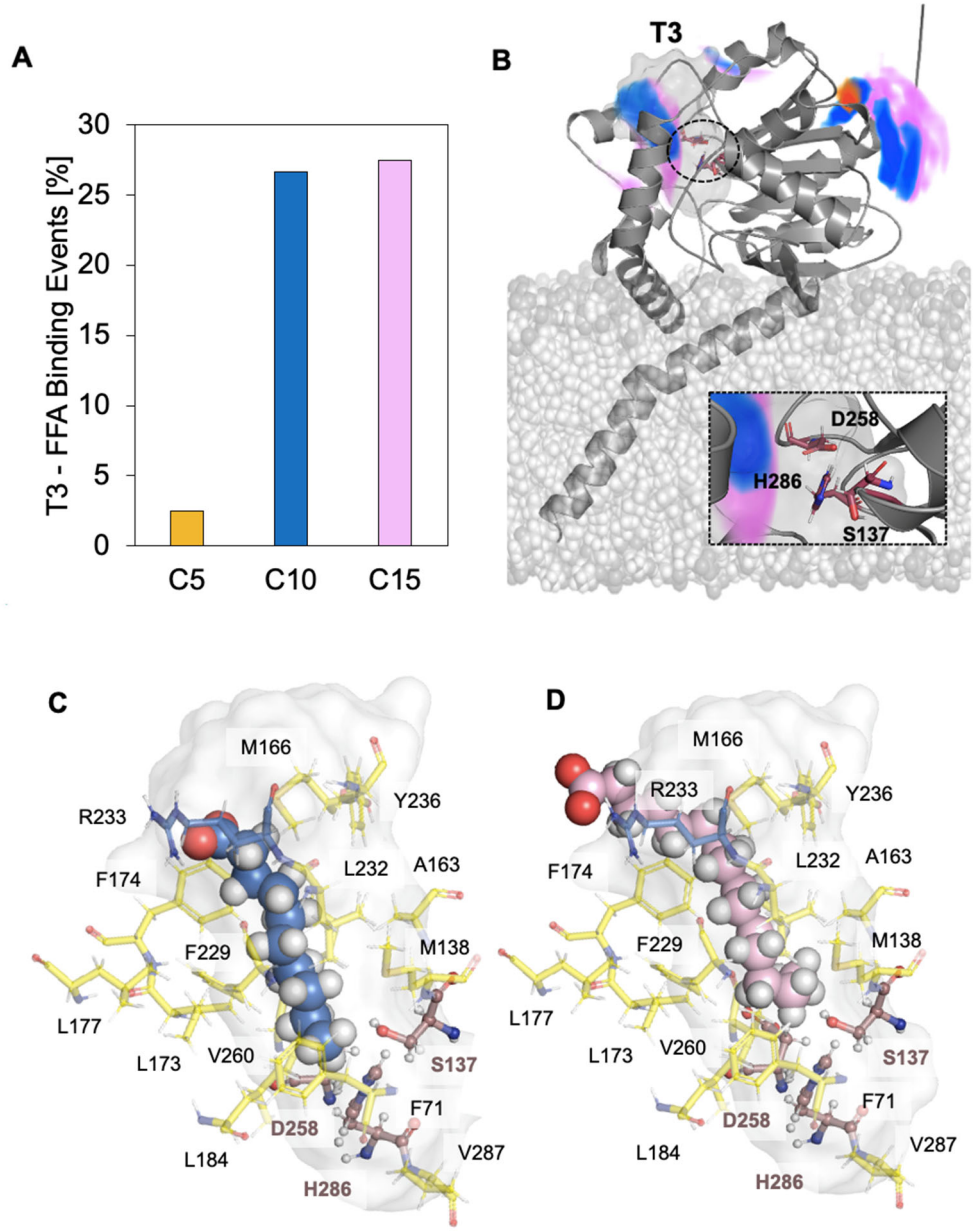

Figure 6. Free ligand diffusion MD simulations show access of FFA molecules to T3. (A) Binding events of C5 (orange), C10 (blue), and C15 (pink) FFAs to T3. Bound FFA poses were selected using a cut-off of 15 Å from the COM of K170, Q234, and Y236, considered as T3 entrance. **(B) 3D density maps representing the probability density of the valeric acid (C5, orange), capric acid (C10, blue), and pentadecanoic acid (C15, magenta) positions around t-PlaF (grey cartoon representation)**. The entire FFA was used in the density map calculations. The colors scale is compatible to panel (A). The FFA poses were clustered during the free ligand diffusion MD simulations**.** T3 is represented with a grey surface and was computed using CAVER 3.0. The catalytic triad is reported as purple sticks in the dashed box. **(C) The representative binding mode of C10 of the top cluster of C10 inside T3**; the cluster comprises 51.8 ± 0.3% of all bound C10 configurations. T3 was computed with CAVER 3.0 and represented as a grey surface. The C10 fatty acid is shown with blue spheres. The catalytic triad is shown with brown spheres. The rest of the T3 residues are shown with yellow sticks, except for R233 reported with blue sticks. **(D) The representative binding mode of C15 of the top cluster of C15 inside T3**; the cluster comprises 54.3 ± 0.3% of all bound C15 configurations. The C15 fatty acid is reported with pink spheres; all else is as in panel C.

2.7 Tail-first Access of C10 into T3 is Energetically Favorable

As a prerequisite to computing the energetics of binding of C10 to the T3 of PlaF, we validated if C10 access via the tail is favorable. We applied steered MD (sMD) simulations (27) to pull FFAs from the bound state obtained during FLD MD simulations (2.4) to the unbound state outside T3. The transition pathway will be later used to define reference points for umbrella sampling (US) simulations to compute a PMF of tunnel egress. A bound FFA (**Table S3** (t-PlaF(III): CAP-1127)) of replica 4 of the FLD MD simulations was chosen as a representative pose. The terminal carbon atom of C10 was considered for pulling from a distance of 3.4 Å to the catalytic oxygen of S137 to 13.1 Å, where it is in the solvent. The FFA was pulled through four consecutive virtual points **(Figure 7B)**; the virtual points were chosen such that the entire egress pathway was described as done before (11). The distance between the pulled C-terminal carbon atom and the virtual point was used as a reaction coordinate. For each step, we repeated the pulling 50 times and computed the work done as a function of the reaction coordinate, as done in previous work (11). By applying Jarzynski's relation (eq. 1) (28), the work was related to the free energy difference between the respective two states along the transition pathway.

$$\overline{e^{-W/kT}} = e^{-\Delta F/kT} \quad (1)$$

The sMD trajectory whose work-*versus*-reaction coordinate profile is closest to the Jarzynski average was identified as the most favorable transition pathway (11) **(Figure S14)**. Its endpoint provided the starting point for the sMD simulations in the next part of the transition pathway. As a result, the transition pathway is close to the lowest-free energy pathway of fatty acid egress from the catalytic site to the periplasmic space. Overall, this approach is the reversed version of sampling unbinding trajectories of ligands from proteins before applying Jarzynski's relation (29-31) but uses piecewise sMD simulations along the pathway to account for the curvilinear tunnel. A total of 1.15 µs of sMD simulation time was used for T3.

PMFs were computed from US simulations along the above-determined transition pathway (19) and post-processed with WHAM (32, 33) to evaluate the energetics of fatty acid egress. As a reaction coordinate, the distance between the terminal carbon atom of C10 to the side-chain oxygen of the catalytic residue S137 was used. 24 windows were sampled with 260 ns of sampling time each, of which the first 100 ns were discarded as equilibration. In both cases, the kernel densities showed a median overlap of 33.6 ± 3.1% between contiguous windows, well suited for PMF calculations (21). The PMF of tunnel egress is converged and precise **(Figure S10)**. It reveals the presence of an energetic global minimum associated with the bound state (state I in **Figure 7B**), which is ~4 kcal mol^{-1} more favorable than the unbound state (state IV in **Figure 7B**), with a binding free energy ΔG°_{comp} = -3.17 ± 0.15 kcal mol^{-1} for the fatty acid computed according to eq. 2 (11) (20) **(Figure 7A)**. Hence, tail-first access of C10 to T3 is energetically favorable. The presence of the FFA in T3 can prevent that T3 is occupied by a fatty acid tail of a GPL or lysophospholipid from the opposite direction, as was suggested previously as a prerequisite for the ester group to reach the catalytic residues (11).

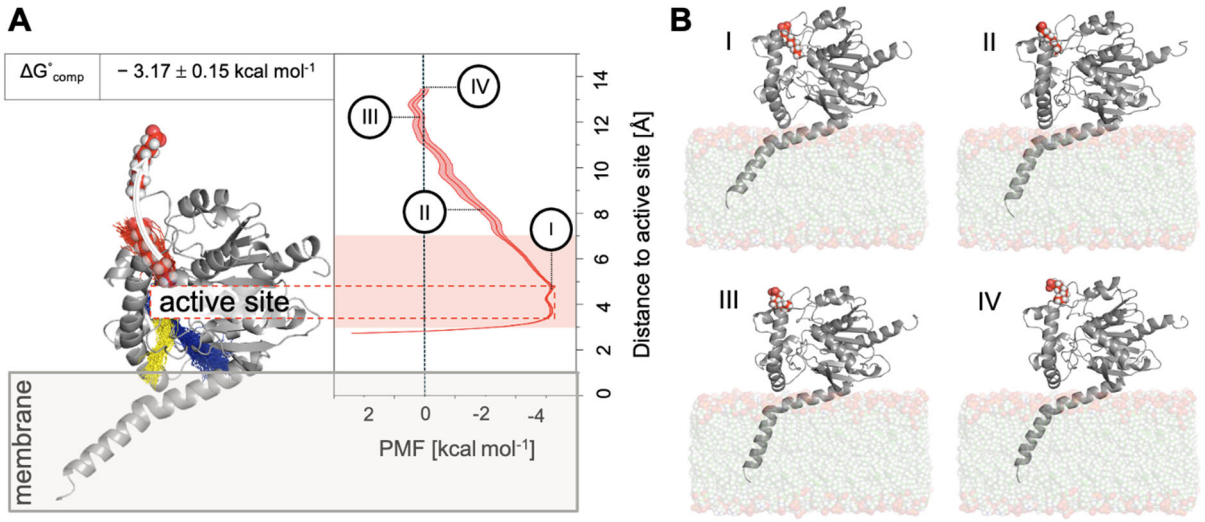

Figure 7. PMF profile of C10 egress through T3 in the t-PlaF configuration (A) and corresponding states (B). The entrance of tunnel T3 is located > 35 Å above the membrane, pointing into the periplasmic space. C10 is pulled from the bound state through T3 into the water phase mimicking the periplasmic space. The catalytic site is marked with a dotted red box. The red-shaded area around the curve represents the SEM. The red-shaded box corresponds to the integration limits used to calculate K_{eq} (eq. 2 (11) (20)) to determine ΔG°_{comp} (see 4.12). State I: Starting position of C10 (in the bound state). State II: C10 tail reaches half of the tunnel. State III: C10 tail is close to the tunnel interface with the periplasmic space. State IV: C10 reaches the end of the T3. The C10 molecule is surrounded by water.

2.8 Tryptophan Substitutions in T3 are suggested to Block FFA Access

To validate the prediction that T3 is the preferred pathway for FFA entering from the water phase, we used Trp substitutions within T3 previously identified (11) that should constrict the tunnel and, thus, block competitive PlaF inhibition. Earlier, this strategy was used to block tunnels of dehalogenases (34) and PlaF (11) with respect to substrate access. The PlaF variants had been predicted such that they minimize the structural destabilization due to a Trp substitution and preferentially occur at sites within T3 that influence the tunnel's geometry (**Table 1**) (11). To strengthen the impact on the tunnel geometry, double substitutions were selected in addition to single ones (**Table S5**).

We then performed MD simulations of free ligand diffusion of C10 to register binding events to T3. C10 was considered bound if the criteria described in section 2.5 are fulfilled. The results revealed a decrease in the C10 binding to T3 in the single Trp variants compared to wildtype, which decreased further in the double variants (**Table 1**). Only a few binding events were observed for the double variants (7/120 for M166W-R233W and 8/120 for M166W-Y236W). In both the double variants, the tunnel is apparently too narrow to allow for C10 binding.

391 **TABLE 1. Characteristics of PlaF variants identified from MD simulations of t-PlaF.**

PlaF variant	Occurrence[a]	Average bottleneck radius[b,c]	Average length[b,c]	C10 binding events[d]
WT	27.75	2.29 ± 0.32	15.16 ± 3.74	26.67
L177W	28.37	1.70 ± 0.34	18.51 ± 3.91	15.83
F229W	24.78	1.67 ± 0.31	17.77 ± 3.71	18.52
M166W_R233W	21.20	1.62 ± 0.30	17.82 ± 3.89	8.33
M166W_Y236W	23.75	1.69 ± 0.30	18.98 ± 3.47	9.33

392 [a] Frequency of occurrence of C10 binding to T3; in %.
393 [b] Data was calculated with CAVER using a probe radius of 1.2 Å.
394 [c] In Å; in addition to the average, the SD is given.
395 [d] Proportion of binding of C10 to the T3 entrance (COM of K170, Q234, Y236) along 1 μs of FLD MD simulations across
396 12 different replicas; in %.
397
398
399 3. DISCUSSION

400 In this study, we assessed at the atomistic level how FFAs localized in different cell compartments can
401 interact with active and inactive configurations of PlaF and how this may regulate *PlaF* activity.

402 Initially, we probed how FFAs can regulate the PlaF dimer-to-monomer and tilting transitions when
403 they are localized in the upper membrane leaflet. Our MD simulations indicate that FFAs stabilize the
404 inactive d-PlaF configuration, which is in accordance with DMP-crosslinking experiments (5).
405 Surprisingly, we found evidence that the FFAs also favor the t-PlaF configuration and facilitate the
406 tilting process. The latter may be explained by a potential reduction of the membrane viscosity when
407 small FFAs are added as membrane components (35). This non-specific effect may also explain why
408 the chain length of the FFA (C10 versus C14) barely affects the tilting. Based on computed free energies
409 of association and tilting, and taking into account the concentration range of PlaF in *P. aeruginosa*, PlaF
410 preferentially exists as inactive d-PlaF in the cytoplasmic membrane in the presence of FFAs. Thereby,
411 higher C10 concentrations stabilize d-PlaF more. The stabilization is likely due to favorable interactions
412 of FFAs with predominantly positively charged residues exclusively located in the lid-like domain of
413 PlaF.

414 Previously, we showed that FFAs inhibit PlaF activity according to a mixed inhibition kinetics
415 mechanism (5). The effects on PlaF dimerization and tilting due to FFAs located in the upper leaflet
416 can contribute to the non-competitive component of this mechanism. To scrutinize if FFAs localized in
417 the water phase (equivalent to the periplasmic space in *P. aeruginosa*) can exert a competitive
418 inhibition, we performed FLD simulations. They showed that C10 and C15 FFAs can bind to active t-
419 PlaF via T3 previously identified (11) with energetically favorable tail-first access. The FFA tail can
420 reach close to the catalytic triad, which may interfere with substrate binding. C5 FFAs showed almost
421 no binding. Notably, these results are concordant with our previous experimental results that medium-
422 chain length FFAs added to *P. aeruginosa* cells inhibit PlaF, whereas no inhibitory effect was shown
423 for shorter FFAs (5). FLD simulations of previously characterized Trp substitutions in T3 (11) suggest
424 that such substitutions block FFA access.

425 In summary, unbiased and biased MD simulations and free energy computations suggest that medium-
426 chain length FFAs can inhibit PlaF competitively and non-competitively, in line with previous
427 experiments (5): They stabilize inactive d-PlaF when localized in the upper membrane leaflet and enter
428 T3 when localized in the periplasmic space. Notably, our study explicitly suggests mutations for either
429 case to probe these effects experimentally. Our findings support the suggestion from *in vivo* results
430 shown here and *in vitro* results presented previously (5) that PlaF activity may be regulated through a

431 product-feedback mechanism. They also open up new perspectives on how to inhibit PlaF, which has
432 been suggested as a promising target for developing new antibiotics against *P. aeruginosa* (5).

433

434 ## 4. MATERIALS AND METHODS

435 ### 4.1 Gas chromatography-mass spectrometric (GC-MS) analysis of FAs extracted from *P.*
436 *aeruginosa*

437 *P. aeruginosa* PA01 (wild-type, WT) and the Δ*plaF* mutant were cultivated overnight (37 ℃, LB
438 medium, agitation), and cells were separated from the supernatant, followed by chloroform/methanol
439 extraction of FFAs, derivatization of FFAs with trimethylsilyl, and quantification by GC-MS as
440 described in ref. (36).

441 ### 4.2 Preparation of Starting Structures

442 The crystal structure of the PlaF dimer is available in the Protein Data Bank (PDB ID 6I8W) (37). The
443 last five residues of the C-terminus of each monomer missing in the structure were added using
444 MODELLER (38), and all small molecule ligands were removed. The dimer was oriented in the
445 membrane using the PPM server (di-PlaF) (17). From that, the "split" s-PlaF configuration of chain A
446 was generated by removing chain B from the dimer orientation. Additionally, chain A was oriented
447 using the PPM server, resulting in the tilted configuration t-PlaF. These three starting configurations,
448 di-PlaF, s-PlaF, and t-PlaF, were embedded into a DOPE:DOPG=3:1 membrane (39) and solvated using
449 PACKMOL-Memgen (40, 41). The membrane composition resembles that of the native inner
450 membrane of Gram-negative bacteria (39).
451 Free fatty acids (FFA) of different chain lengths were added as upper-leaflet components in the
452 protonated form (42) in two different concentrations; here, "upper" refers to the leaflet pointing to the
453 periplasmic space. A distance of at least 15 Å between the protein or membrane and the solvent box
454 boundaries was kept. To obtain a neutral system, counter ions were added that replaced solvent
455 molecules (KCl 0.15 M). The generated systems are summarized in **Table S3**. The size of the resulting
456 systems was ∼140,000 atoms for s-PlaF and t-PlaF and ∼185,000 atoms for di-PlaF.

457 ### 4.3 Unbiased Molecular Dynamics Simulations of PlaF Monomers

458 The GPU particle mesh Ewald implementation from the AMBER21 suite of molecular simulation
459 programs (43) with the ff14SB (44) and Lipid14/17 forcefields (45, 46) for the protein and the
460 membrane lipids, respectively, were used; water molecules and ions were parametrized using the TIP3P
461 model (47) and the Li and Merz 12-6 ions parameters (48, 49). For the monomer configurations (s-PlaF
462 and t-PlaF), 12 independent simulations of 1 μs length were performed (**Table S3**). Covalent bonds to
463 hydrogens were constrained with the SHAKE algorithm (50) in all simulations, allowing the use of a
464 time step of 2 fs. Details of the thermalization of the simulation systems are given below. All unbiased
465 MD simulations showed stable protein structures and membrane phases evidenced by electron density
466 calculations (**Table S3, Figures S2-S5**).

467 ### 4.4 Relaxation, Thermalization, and Production Runs of the Plaf Monomers.

468 An initial minimization step was performed with the CPU code of pmemd (51). Each minimization was
469 organized in four steps of 1000 cycles each, for a total of 4000 cycles of minimization. Afterward, each
470 minimized system was thermalized in one stage from 0 to 300 K over 25 ps using the NVT ensemble

471 and the Langevin thermostat (52), and the density was adapted to 1.0 g cm^{-3} over 975 ps using the NPT
472 ensemble with a semi-isotropic Berendsen barostat (53) with the pressure set to 1 bar. The
473 thermalization and equilibration were performed with the GPU code of pmemd (51). There are three
474 density equilibration steps with a total time of 4 ns. The sum of thermalization, density adaptation, and
475 equilibration takes 5 ns.
476 For each replica, 1 μs of production run using the GPU code of pmemd was performed in the NPT
477 ensemble at a temperature of 300 K using the Langevin thermostat (52) and a collision frequency of
478 1 ps^{-1}. To avoid noticeable distortions in the simulation box size, semi-isotropic pressure scaling using
479 the Berendsen barostat (53) and a pressure relaxation time of 1 ps was employed by coupling the box
480 size changes along the membrane plane (54).

481 ### 4.5 Analysis of MD Trajectories of the PlaF Monomer

482 The trajectories were analyzed with CPPTRAJ (25). As in ref. (5), the angle between the membrane
483 normal and the vector between the COM of residues 21–25 and residues 35–38 was calculated to
484 describe the tilting of monomeric PlaF.

485 ### 4.6 PMF and Free Energy Calculation of Dimer Dissociation

486 For calculating a configurational free energy profile (PMF) of dimer separation, 71 intermediate states
487 were generated by separating one chain of the dimer along the membrane plane in steps of 0.5 Å,
488 respectively. The generated structures represent the separation process of the PlaF dimer. To sample
489 configurations along the chain separation in a membrane environment, each intermediate state was
490 embedded into a membrane of approximately 157x157 Å by using PACKMOL-Memgen (41) (see
491 chapter 4.2 and **Table S3** for the composition of the systems). Each intermediate state was minimized,
492 thermalized, and equilibrated following the protocol already described (sections 4.2 and 4.3).
493 Umbrella sampling simulations were performed starting from each equilibrated intermediate state by
494 restraining the initial distance between chains in every window with a harmonic potential, using a force
495 constant of 4 kcal mol^{-1} $Å^{-2}$ (19); the distance between the COM of C_α atoms of residues 25-38 of each
496 monomer was used as a reaction coordinate value *r*. Independent MD simulations of 800 ns in length
497 each were started from each intermediate state, resulting in a total simulation time of 56.8 μs. *r* was
498 recorded every 2 ps and post-processed with the Weighted Histogram Analysis Method implementation
499 of A. Grossfield (WHAM 2.0.9)(32), removing the first 640 ns as an equilibration phase of the system.
500 The error was estimated by considering the last 160 ns only and by calculating the standard error of the
501 mean from eight independent free energy profiles determined every 20 ns during this time. The overlap
502 between contiguous windows and the convergence of the PMFs was validated **(Figures S8-9)**. The
503 association free energy was estimated from the obtained PMF following the membrane two-body
504 derivation (23) and our previous work (5, 22) (eqs. S1-4).

505 ### 4.7 PMF and Free Energy Calculation of Monomer Tilting

506 The initial conformations used in every window for calculating the PMF of the monomer tilting were
507 obtained from the first microsecond of MD simulations of replica 2 of s-PlaF in the Tilt1 system **(Table**
508 **S3).** Oriented as in the di-PlaF crystal structure, the monomer spontaneously tilted. The distance *d* along
509 the z-axis between the COM of C_α atoms of residues 33-37 of the monomer with the membrane center
510 was used to select 40 intermediate tilting configurations as done already with a standard membrane
511 composition (5). The starting conformations were extracted from the representative trajectory, taking
512 the respective snapshots where *d* showed the least absolute deviation to the average value obtained by

513 binning *d* in windows of 0.5 Å width and with an evenly distributed separation of 0.5 Å. *d* was restrained
514 for every configuration by a harmonic potential with a force constant of 4 kcal mol^{-1} $Å^{-2}$, and sampling
515 was performed for 800 ns per window. *d* values were obtained every 2 ps and analyzed as described
516 above. The error was estimated in the same way as for the dimerization. The overlap between
517 contiguous windows and the convergence of the PMF was validated **(Figure S7)**. The free energy of
518 monomer tilting was estimated from the obtained PMF following protocols explained in previous works
519 (5, 20) (eq. S5-6).
520 The dissociation and tilting equilibrium constants as well as the proportion of PlaF dimer versus
521 monomer in a live cell of *P. aeruginosa* were calculated in the same way as in ref. (5).
522
523 4.8 Density Maps of Free Fatty Acids Binding to d-PlaF in the Membrane
524
525 The structure of the PlaF dimer was embedded in a phospholipid membrane with the composition
526 DOPE:DOPG 3:1 following the protocol described in section 4.1. C10 fatty acids were added as
527 membrane upper leaflet components in the protonated configuration (42). The final composition of the
528 upper leaflet is DOPE:DOPG:C10 3:1:1. Unbiased MD simulations of the system were performed
529 following the protocol used for the monomers (see sections 4.2 and 4.3). From the obtained trajectories,
530 all FFA binding poses were identified in which FFAs have an RMSD < 1.5 Å to the previous frame (see
531 Supplementary results) and are located at most 6 Å away from the protein. These binding poses were
532 clustered using the hierarchical agglomerative (bottom-up) algorithm implemented in cpptraj (25),
533 using the minimum distance ε between the clusters as the cluster criterion. Starting from ε = 2.0 Å, we
534 gradually increased ε in 0.5 Å intervals until the population of the largest cluster remained unchanged
535 (ε = 5.0 Å). We calculated the density maps of the fatty acids considering all atoms using the grid
536 function available in CPPTRAJ and a grid spacing of 1.5 Å (25).

537 4.9 Free Ligand Diffusion Simulations (FLDs) to study FFA Binding from the Water Phase
538 to t-PlaF

539 t-PlaF was embedded in a phospholipid membrane with the composition DOPE:DOPG 3:1 following
540 the protocol described in section 4.1. To investigate the binding of FFAs to PlaF, 1 µs long MD
541 simulations of the free diffusion of FFA molecules located in the water phase were performed to
542 investigate their binding to t-PlaF. We considered three independent systems (see **Table S3** in which
543 ten FFA molecules of specified acyl chain length each, namely, valeric acid (VAL-C5), capric acid
544 (CAP-C10), and pentadecanoic acid (PEN-C15), are in the deprotonated configuration, resulting in a
545 concentration of ~30 mM in the corresponding solvation box. The eventual formation of aggregates
546 was checked by visual inspection of the trajectories. 12 replicas of 1 µs simulation length were run for
547 each system. The minimization, thermalization, equilibration, and production schemes are like the ones
548 performed in sections 4.2 and 4.3. To identify the most likely binding epitopes, we computed probability
549 densities of the location of either fatty acid. Stably bound conformations (see chapter 2.6 for a
550 definition) were clustered to extract the most representative binding poses.

551 4.10 Simulated Extraction of Fatty Acids through T3

552 MD simulations were performed using the GPU implementation of the AMBER 21 molecular
553 simulation package (55), employing the same protocol as in chapters 4.3 and 4.4. To extract an FFA
554 from T3 into the periplasmic space, we selected a bound FFA (**Table S3** (t-PlaF(III): CAP-1127)) of
555 replica 4 of the FLD MD simulations as a representative pose. We pulled it by its terminal carbon atom
556 from the catalytic center to the tunnel's exit using constant velocity sMD simulations, with a constant

velocity of 1 Å ns^{-1} and a force constant of 5 kcal mol^{-1} $Å^{-2}$ (27, 31). Pulling simulations at low velocities have been used with lipids to calculate free energy profiles (11, 55). Using low pulling rates, the lipids have time to adapt to energetically favorable conformations during the extraction process. T3 was divided into consecutive fragments connected to T3 pulling points generated by the COM of specific amino acid residues (**Table S4**). We performed 50 replicas for each pulling simulation to identify the lowest energy pathway. The work was computed as a function of the reaction coordinate. The computed work was further related to the free energy difference between two states of the pulling simulation by applying Jarzynski's relation (eq. 1) (28). ΔF is the free energy difference between two states, which is connected to the work W done on the system. k is the Boltzmann constant, and T is the absolute temperature of the system. The replica closest to Jarzynski's average (28) was considered to describe the lowest free energy pathway and provided the starting point for the next pulling stage, as done in ref. (11). This procedure results in faster convergence of PMF profiles subsequently computed along the pathway, decreasing the overall computation needed (29).

4.11 Umbrella Sampling Simulations and PMF calculations

To understand the energetic contribution associated with the binding of C10 molecules to T3, PMFs were computed based on umbrella sampling, taking structures from the sMD simulations (see chapter 4.10) as starting points. As a reaction coordinate, the distance of the terminal carbon atom of the FFA to the hydroxyl oxygen of S137 of the active site was used. Consecutive positions of the FFA from the bound state to the periplasmic space, as determined in chapter 4.10, were considered reference points, defining the umbrella windows. To achieve sufficient overlap between the umbrella windows, distances between reference points of 0.5 Å were used. The length of T3 and the size of the FFA can vary. Therefore, for sampling the egress of the bound fatty acid, different numbers of windows were required for the tunnel. The FFA was restrained by harmonic potentials to the reference points, using a force constant of 5 kcal mol^{-1} $Å^{-2}$. To achieve sufficient convergence of the PMF profile **(Figure S10)**, each window was sampled for 260 ns, of which the last 160 ns were used to calculate the PMF. Distance values were recorded every 2 ps and processed with WHAM (32). The PMFs were evaluated for convergence by checking the change in the free energy profile with increasing sampling time in steps of 20 ns **(Figure S10)**.

4.12 Absolute Binding Free Energy from the PMF

The absolute binding free energy of substrates to PlaF was determined from the computed PMF using an approach modified (11) from Chen and Kuyucak (21). The PMF was integrated along the reaction coordinate (eq. 2) to calculate an association (equilibrium) constant (K_{eq}).

$$K_{eq} = \pi r^2 \int_{periplasm}^{active_site} e^{-W(\xi)/k_B T}\, d\xi \qquad (2)$$

Here, r is the maximum bottleneck radius of the respective tunnel, which was determined by CAVER analysis (11, 56), πr^2 is the maximum cross-sectional area of the tunnel, $W(\xi)$ is the PMF at a specific value of the reaction coordinate, k is the Boltzmann constant, and T is the absolute temperature at which the simulations were performed. The integration limits describe the bound state. A reaction coordinate > 7 Å was considered as an unbound state and for this reason not included in the integration.

K_{eq} was then transformed to the mole fraction scale (K_x). For (un)binding to the solution, a standard state of 1 M is considered (20) (eq. 3).

$$K_x = K_{eq} \frac{1\,mol}{1\,l} = K_{eq} \frac{1}{1660\,Å^3} \quad (3)$$

From K_x, the difference in the standard free energy (eq. 4) between the bound and unbound state (ΔG_{comp}°) of a single substrate molecule was calculated.

$$\Delta G_{comp}^{\circ} = -RTln(K_x) \quad (4)$$

4.13 Blocking Access of the Fatty Acid to T3.

To verify the prediction that FFA can bind to T3 and, thereby, inhibit PlaF, we intended to block T3 with small-to-tryptophan substitutions of tunnel-lining residues, following an approach already pursued (11). The selected residues were substituted to tryptophan using FoldX (57), and the stability of the PlaF variants was evaluated in terms of the change in folding free energy ($\Delta\Delta G$) with respect to the wildtype (58). Single and double amino acid substitutions were performed 10 times for each residue or residue couple, and the results were averaged. If the average $\Delta\Delta G > 3$ kcal mol^{-1}, the substitution is considered destabilizing (59) and was not further pursued. To check if the proposed substitutions will block the tunnel, the bottleneck radius of the variant tunnels was calculated using CAVER 3.0 (56). The COM of the catalytic residues S137 and H286 was defined as the starting points of the search as done in our previous work (11). The probe radius was set to 2 Å.
Mutant FLD MD simulations and binding free energy calculations of C10 to T3 were performed by following the same protocols described for the wild type.

5 ACKNOWLEDGEMENTS

This study was funded by the Deutsche Forschungsgemeinschaft (DFG, German Research Foundation) project no. 267205415 / CRC1208 grant to F.K. and K.-E.J. (TP A02) and H.G. (TP A03). We are grateful for computational support by the "Zentrum für Informations und Medientechnologie" at the Heinrich-Heine-Universität Düsseldorf and the computing time provided by the John von Neumann Institute for Computing (NIC) to H.G. on the supercomputer JUWELS at Jülich Supercomputing Centre (JSC) (user IDs: HDD18; plaf) and to Muttalip Caliskan (Institute of Molecular Enzyme Technology, Heinrich Heine University Düsseldorf) for experimental support.

6 AUTHOR CONTRIBUTIONS

R.G. computational investigation, analysis, visualization; M.M., B.T. experimental investigation, analysis, visualization, K.-E.J., F.K., H.G. conceptualization, supervision, analysis, funding, resources, project management. The manuscript was written with the contributions of all authors. All authors have given approval for the final version of the manuscript.

7 CONFLICT OF INTEREST STATEMENT

The authors declare no conflicts of interest.

8 DATA and SOFTWARE AVAILABILITY

The AMBER21 source code is available at http://ambermd.org/.

637 REFERENCES

638

639 1. Gellatly SL, Bains M, Breidenstein EBM, Strehmel J, Reffuveille F, Taylor PK, et al. Novel roles for
640 two-component regulatory systems in cytotoxicity and virulence-related properties in Pseudomonas aeruginosa.
641 AIMS Microbiol. 2018;4(1):173-91.
642 2. Gellatly SL, Hancock RE. Pseudomonas aeruginosa: new insights into pathogenesis and host defenses.
643 Pathog Dis. 2013;67(3):159-73.
644 3. Hauser AR. Pseudomonas aeruginosa: so many virulence factors, so little time. Crit Care Med.
645 2011;39(9):2193-4.
646 4. Songer JG. Bacterial phospholipases and their role in virulence. Trends Microbiol. 1997;5(4):156-61.
647 5. Bleffert F, Granzin J, Caliskan M, Schott-Verdugo SN, Siebers M, Thiele B, et al. Structural,
648 mechanistic, and physiological insights into phospholipase A-mediated membrane phospholipid degradation in
649 Pseudomonas aeruginosa. Elife. 2022;11.
650 6. Chwastek G, Surma MA, Rizk S, Grosser D, Lavrynenko O, Rucinska M, et al. Principles of Membrane
651 Adaptation Revealed through Environmentally Induced Bacterial Lipidome Remodeling. Cell Rep.
652 2020;32(12):108165.
653 7. Hishikawa D, Hashidate T, Shimizu T, Shindou H. Diversity and function of membrane
654 glycerophospholipids generated by the remodeling pathway in mammalian cells. J Lipid Res. 2014;55(5):799-
655 807.
656 8. Benamara H, Rihouey C, Abbes I, Ben Mlouka MA, Hardouin J, Jouenne T, et al. Characterization of
657 membrane lipidome changes in Pseudomonas aeruginosa during biofilm growth on glass wool. PLoS One.
658 2014;9(9):e108478.
659 9. Chipot C. Free energy calculations applied to membrane proteins. Methods Mol Biol. 2008;443:121-44.
660 10. Lotz SD, Dickson A. Unbiased Molecular Dynamics of 11 min Timescale Drug Unbinding Reveals
661 Transition State Stabilizing Interactions. J Am Chem Soc. 2018;140(2):618-28.
662 11. Ahmad S, Strunk CH, Schott-Verdugo SN, Jaeger KE, Kovacic F, Gohlke H. Substrate Access
663 Mechanism in a Novel Membrane-Bound Phospholipase A of Pseudomonas aeruginosa Concordant with
664 Specificity and Regioselectivity. J Chem Inf Model. 2021;61(11):5626-43.
665 12. Martinez E, Orihuela CJ, Campos-Gomez J. Pseudomonas aeruginosa Secretes the Oxylipin Autoinducer
666 Synthases OdsA and OdsB via the Xcp Type 2 Secretion System. J Bacteriol. 2022;204(7):e0011422.
667 13. Liu L, Li T, Cheng XJ, Peng CT, Li CC, He LH, et al. Structural and functional studies on Pseudomonas
668 aeruginosa DspI: implications for its role in DSF biosynthesis. Sci Rep. 2018;8(1):3928.
669 14. Monje-Galvan V, Warburton L, Klauda JB. Setting Up All-Atom Molecular Dynamics Simulations to
670 Study the Interactions of Peripheral Membrane Proteins with Model Lipid Bilayers. Methods Mol Biol.
671 2019;1949:325-39.
672 15. Genheden S, Ryde U. The MM/PBSA and MM/GBSA methods to estimate ligand-binding affinities.
673 Expert Opin Drug Discov. 2015;10(5):449-61.
674 16. Frieg B, Gremer L, Heise H, Willbold D, Gohlke H. Binding modes of thioflavin T and Congo red to the
675 fibril structure of amyloid-beta(1-42). Chem Commun (Camb). 2020;56(55):7589-92.
676 17. Lomize MA, Pogozheva ID, Joo H, Mosberg HI, Lomize AL. OPM database and PPM web server:
677 resources for positioning of proteins in membranes. Nucleic Acids Res. 2012;40(Database issue):D370-6.
678 18. Lomize MA, Lomize AL, Pogozheva ID, Mosberg HI. OPM: orientations of proteins in membranes
679 database. Bioinformatics. 2006;22(5):623-5.
680 19. G.M. Torrie JPV. Nonphysical sampling distributions in Monte Carlo free-energy estimation: Umbrella
681 sampling. Journal of Computational Physics. 1977;23(2):187-99.
682 20. Doudou S, Burton NA, Henchman RH. Standard Free Energy of Binding from a One-Dimensional
683 Potential of Mean Force. J Chem Theory Comput. 2009;5(4):909-18.
684 21. Chen PC, Kuyucak S. Accurate determination of the binding free energy for KcsA-charybdotoxin
685 complex from the potential of mean force calculations with restraints. Biophys J. 2011;100(10):2466-74.
686 22. Pagani G, Gohlke H. On the contributing role of the transmembrane domain for subunit-specific
687 sensitivity of integrin activation. Sci Rep. 2018;8(1):5733.
688 23. Johnston JM, Wang H, Provasi D, Filizola M. Assessing the relative stability of dimer interfaces in g
689 protein-coupled receptors. PLoS Comput Biol. 2012;8(8):e1002649.
690 24. Bleffert F, Granzin J, Gohlke H, Batra-Safferling R, Jaeger KE, Kovacic F. Pseudomonas aeruginosa
691 esterase PA2949, a bacterial homolog of the human membrane esterase ABHD6: expression, purification and
692 crystallization. Acta Crystallogr F Struct Biol Commun. 2019;75(Pt 4):270-7.
693 25. Roe DR, Cheatham TE, 3rd. PTRAJ and CPPTRAJ: Software for Processing and Analysis of Molecular
694 Dynamics Trajectory Data. J Chem Theory Comput. 2013;9(7):3084-95.
695 26. Hossain MS, Berg S, Bergstrom CAS, Larsson P. Aggregation Behavior of Medium Chain Fatty Acids
696 Studied by Coarse-Grained Molecular Dynamics Simulation. AAPS PharmSciTech. 2019;20(2):61.

27. Izrailev SS, S.; Isralewitz, B.; Kosztin, D.; Lu, H.; Molnar, F.; Wriggers, W.; Schulten, K. Steered Molecular Dynamics. Computational Molecular Dynamics: Challenges, Methods, Ideas. 1999:39−65.
28. Jarzynski C. Nonequilibrium equality for free energy differences. Phys Rev Lett. 1997;78(14):2690-3.
29. Bureau HR, Merz DR, Jr., Hershkovits E, Quirk S, Hernandez R. Constrained Unfolding of a Helical Peptide: Implicit versus Explicit Solvents. PLoS One. 2015;10(5):e0127034.
30. Homeyer N, Stoll F, Hillisch A, Gohlke H. Binding Free Energy Calculations for Lead Optimization: Assessment of Their Accuracy in an Industrial Drug Design Context. Journal of Chemical Theory and Computation. 2014;10(8):3331-44.
31. Izrailev S, Crofts AR, Berry EA, Schulten K. Steered molecular dynamics simulation of the Rieske subunit motion in the cytochrome bc(1) complex. Biophys J. 1999;77(4):1753-68.
32. Grossfield A. WHAM: the weighted histogram analysis method. http://membraneurmcrochesteredu/wordpress/? 2016;version 2.0.9.
33. Zhu F, Hummer G. Convergence and error estimation in free energy calculations using the weighted histogram analysis method. J Comput Chem. 2012;33(4):453-65.
34. Biedermannova L, Prokop Z, Gora A, Chovancova E, Kovacs M, Damborsky J, et al. A single mutation in a tunnel to the active site changes the mechanism and kinetics of product release in haloalkane dehalogenase LinB. J Biol Chem. 2012;287(34):29062-74.
35. Hac-Wydro K, Wydro P. The influence of fatty acids on model cholesterol/phospholipid membranes. Chem Phys Lipids. 2007;150(1):66-81.
36. Weiler AJ, Spitz O, Gudzuhn M, Schott-Verdugo SN, Kamel M, Thiele B, et al. A phospholipase B from Pseudomonas aeruginosa with activity towards endogenous phospholipids affects biofilm assembly. Biochim Biophys Acta Mol Cell Biol Lipids. 2022;1867(4):159101.
37. Berman HM, Westbrook J, Feng Z, Gilliland G, Bhat TN, Weissig H, et al. The Protein Data Bank. Nucleic Acids Res. 2000;28(1):235-42.
38. Sali A, Blundell TL. Comparative protein modelling by satisfaction of spatial restraints. J Mol Biol. 1993;234(3):779-815.
39. Murzyn K, Rog T, Pasenkiewicz-Gierula M. Phosphatidylethanolamine-phosphatidylglycerol bilayer as a model of the inner bacterial membrane. Biophys J. 2005;88(2):1091-103.
40. Martinez L, Andrade R, Birgin EG, Martinez JM. PACKMOL: a package for building initial configurations for molecular dynamics simulations. J Comput Chem. 2009;30(13):2157-64.
41. Schott-Verdugo S, Gohlke H. PACKMOL-Memgen: A Simple-To-Use, Generalized Workflow for Membrane-Protein-Lipid-Bilayer System Building. J Chem Inf Model. 2019;59(6):2522-8.
42. Pashkovskaya AA, Vazdar M, Zimmermann L, Jovanovic O, Pohl P, Pohl EE. Mechanism of Long-Chain Free Fatty Acid Protonation at the Membrane-Water Interface. Biophysical Journal. 2018;114(9):2142-51.
43. Salomon-Ferrer R, Gotz AW, Poole D, Le Grand S, Walker RC. Routine Microsecond Molecular Dynamics Simulations with AMBER on GPUs. 2. Explicit Solvent Particle Mesh Ewald. J Chem Theory Comput. 2013;9(9):3878-88.
44. Maier JA, Martinez C, Kasavajhala K, Wickstrom L, Hauser KE, Simmerling C. ff14SB: Improving the Accuracy of Protein Side Chain and Backbone Parameters from ff99SB. J Chem Theory Comput. 2015;11(8):3696-713.
45. Dickson CJ, Madej BD, Skjevik AA, Betz RM, Teigen K, Gould IR, et al. Lipid14: The Amber Lipid Force Field. J Chem Theory Comput. 2014;10(2):865-79.
46. Dickson CJ, Walker RC, Gould IR. Lipid21: Complex Lipid Membrane Simulations with AMBER. J Chem Theory Comput. 2022;18(3):1726-36.
47. Zhao CL, Zhao DX, Bei CC, Meng XN, Li S, Yang ZZ. Seven-Site Effective Pair Potential for Simulating Liquid Water. J Phys Chem B. 2019;123(21):4594-603.
48. Li P, Song LF, Merz KM, Jr. Systematic Parameterization of Monovalent Ions Employing the Nonbonded Model. J Chem Theory Comput. 2015;11(4):1645-57.
49. Sengupta A, Li Z, Song LF, Li P, Merz KM, Jr. Correction to "Parameterization of Monovalent Ions for the OPC3, OPC, TIP3P-FB, and TIP4P-FB Water Models". J Chem Inf Model. 2021;61(7):3734-5.
50. Krautler V, Van Gunsteren WF, Hunenberger PH. A fast SHAKE: Algorithm to solve distance constraint equations for small molecules in molecular dynamics simulations. Journal of Computational Chemistry. 2001;22(5):501-8.
51. Le Grand S, Gotz AW, Walker RC. SPFP: Speed without compromise-A mixed precision model for GPU accelerated molecular dynamics simulations. Comput Phys Commun. 2013;184(2):374-80.
52. Quigley D, Probert MI. Langevin dynamics in constant pressure extended systems. J Chem Phys. 2004;120(24):11432-41.
53. Berendsen HJC, Postma JPM, Gunsteren WFv, DiNola A, Haak JR. Molecular dynamics with coupling to an external bath. The Journal of Chemical Physics. 1984;81(8):3684-90.

54. Lin YQ, Pan DY, Li JM, Zhang LX, Shao XM. Application of Berendsen barostat in dissipative particle dynamics for nonequilibrium dynamic simulation. J Chem Phys. 2017;146(12).
55. Marrink SJ, Berger O, Tieleman P, Jahnig F. Adhesion forces of lipids in a phospholipid membrane studied by molecular dynamics simulations. Biophys J. 1998;74(2 Pt 1):931-43.
56. Chovancova E, Pavelka A, Benes P, Strnad O, Brezovsky J, Kozlikova B, et al. CAVER 3.0: a tool for the analysis of transport pathways in dynamic protein structures. PLoS Comput Biol. 2012;8(10):e1002708.
57. Schymkowitz J, Borg J, Stricher F, Nys R, Rousseau F, Serrano L. The FoldX web server: an online force field. Nucleic Acids Res. 2005;33(Web Server issue):W382-8.
58. Guerois R, Nielsen JE, Serrano L. Predicting changes in the stability of proteins and protein complexes: a study of more than 1000 mutations. J Mol Biol. 2002;320(2):369-87.
59. Tokuriki N, Stricher F, Schymkowitz J, Serrano L, Tawfik DS. The stability effects of protein mutations appear to be universally distributed. J Mol Biol. 2007;369(5):1318-32.

769 Table of Contents Graphic

770

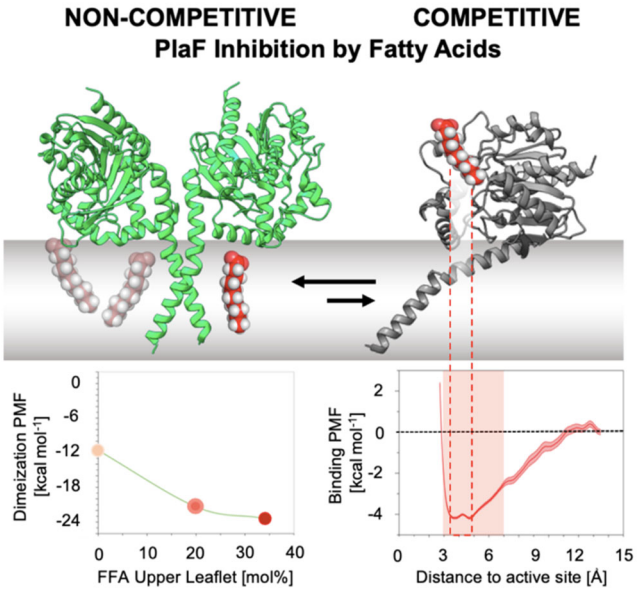

771